Soft Matter

PAPER

View Article Online
View Journal | View Issue

Cite this: *Soft Matter*, 2026, **22**, 2184

Mechanical instabilities in drying protein droplets under substrate-free conditions

Ludovic Pauchard, *[a] Romain Bordes, [b] Cécile Le Floch-Fouéré [c] and Denis Renard [d]

Understanding how proteins of different origins behave during drying is essential for controlling the mechanical stability and final structure of protein-based materials. Here, we examine the drying dynamics of acoustically levitated droplets containing either napin, a plant-derived seed storage protein, or native phosphocaseinate, a dairy protein complex, to uncover how their intrinsic physicochemical and mechanical properties govern evaporation-driven instabilities. Compared to sessile droplets, levitated droplets dry under symmetric evaporation conditions, minimizing substrate effects and contact-line pinning. During drying, both systems develop a solid skin at the air–liquid interface, which undergoes mechanical buckling once compressive stresses exceed the skin's rigidity. Despite similar overall drying kinetics, differences emerge between the two protein systems: native phosphocaseinate droplets form ductile, crack-free shells, whereas napin droplets display brittle fracture and surface cracking. These contrasting behaviours reflect fundamental differences between plant and animal proteins in terms of interfacial activity and network formation. The results are further supported by comparison with model colloid–polymer films, establishing a direct link between interfacial mechanics, crack formation, and film ductility. By revealing how protein origin governs drying-induced instabilities, this work provides mechanistic insight into the design of protein-based materials and supports the development of sustainable, plant-derived protein alternatives for food, pharmaceutical, and soft-material applications.

Received 6th November 2025,
Accepted 11th February 2026

DOI: 10.1039/d5sm01113b

rsc.li/soft-matter-journal

A Introduction

The drying of droplets containing non-volatile solutes gives rise to a wide range of morphological and mechanical instabilities, resulting from the coupling between evaporation, solute transport, and stress development within the drying material. Such phenomena are of major importance in many scientific and industrial contexts, including food processing, pharmaceutical formulations, and soft-matter engineering, where drying is a key step in the fabrication of powders and encapsulated structures. In bio-colloidal systems, drying is particularly complex because proteins for example combine colloidal, interfacial, and mechanical properties that evolve continuously as concentration increases during solvent evaporation.[1]

As a droplet dries, solvent evaporation occurs at the air–liquid interface, inducing internal flows that transport non-volatile components toward the interface to compensate for evaporative losses.[2,3] This redistribution of solutes leads to the formation of concentration gradients, interfacial accumulation, and eventually the development of a solid or gel-like skin. The subsequent mechanical response of this skin—elastic deformation, buckling, or fracture—governs the final morphology of the dried object. Numerous studies have investigated these mechanisms in sessile droplets, where one of the primary parameters influencing the evaporation is the behaviour of the droplet's contact line, which governs the interaction between the liquid phase and the substrate. This contact line may remain pinned or recede during drying, affecting the redistribution of solutes and the emergence of patterns, such as the well-known "coffee ring" effect.[4] The contact angle and the contact base of the droplet play a crucial role in determining evaporation rates, flow patterns, and deposition structures.[2,5–8] In such configurations, contact-line pinning and enhanced evaporation at the droplet edge often lead to radial concentration gradients and edge-initiated solidification, complicating the interpretation of intrinsic material properties.

Drying of protein dispersions has garnered considerable attention over the last few decades. Indeed, proteins constitute a particularly complex class of drying systems because their behaviour depends sensitively on their size, aggregation state, interfacial activity, and ability to form cohesive networks upon

[a] *Université Paris-Saclay, CNRS, FAST, 91405 Orsay, France. E-mail: ludovic.pauchard@cnrs.fr*
[b] *Department of Chemistry and Chemical Engineering, Chalmers University of Technology, Gothenburg 41296, Sweden*
[c] *INRAE, Institut Agro, STLO, 35042 Rennes, France*
[d] *INRAE, UR 1268 Biopolymères Interactions Assemblages, 3 Impasse Yvette Cauchois, La Géraudière, CS 71627, 44316 Nantes Cedex 3, France*

concentration. Previous studies have shown that different proteins can exhibit markedly different drying behaviours, reflecting differences in molecular structure and intermolecular interactions.[3,9,10] However, establishing direct links between protein physicochemical properties and drying-induced mechanical instabilities remains challenging, in part because substrate effects and geometric constraints often dominate the observed dynamics.

In this work, we focus on two protein systems with strongly contrasted physicochemical characteristics: native phosphocaseinate (NPC) and napin (NAP). NPC consists of colloidal assemblies of casein proteins (αs1-, αs2-, β- and K-caseins) and phosphate and calcium ions organized into a micellar assembly whose internal structure has been a matter of controversy for decades.[11–18] These assemblies are highly hydrated and typically organized into soft micellar structures with characteristic sizes ranging from 100 to 300 nm (with a molecular mass of 5×10^5 kg mol^{-1}).[17] In contrast, NAP is a small globular protein with a typical size of about 2 nm (with a molecular mass of 14 kg mol^{-1}),[19] remaining molecularly dispersed in solution. The differences in their size and structure make both systems appropriate and relevant to study systems and assess their influence on droplet–particle conversion.

These differences in colloidal organization and intermolecular interactions are expected to strongly affect drying dynamics. In particular, they should influence (i) the kinetics and homogeneity of protein accumulation at the air–liquid interface, (ii) the structure and mechanical properties of the interfacial skin that forms during evaporation, and (iii) the ability of this skin to relax evaporation-induced stresses through elastic deformation or fracture. Such questions are especially relevant in the context of emerging protein formulations and blends, where understanding the mechanical stability of drying protein systems is essential for process optimization.[20–24]

To access these mechanisms in their intrinsic form, independent of substrate-induced artefacts, we investigate the drying of protein droplets under substrate-free conditions using acoustic levitation. Acoustic levitation offers distinct advantages over traditional sessile geometries by preventing substrate interactions that can influence solute deposition and modify evaporation dynamics.[25] With aloft droplets, evaporation occurs symmetrically across the droplet surface, minimizing contact-line pinning effects and promoting more homogeneous internal flows, conditions that are particularly valuable for understanding the inherent drying properties of protein blends without substrate interference. This method has recently been improved to stabilize small objects over long periods of time, typically the drying timescale.[26,27] This geometry provides a unique framework to follow the formation of an interfacial skin, the progression of a gelation or solidification front, and the onset of mechanical instabilities such as buckling, directly in relation to the interfacial and mechanical properties of the protein system.

By comparing the drying dynamics of levitated NPC and NAP droplets at identical initial concentrations, we show how differences in the colloidal structure and mechanical response translate into distinct drying pathways. While NPC droplets form ductile, crack-free shells, NAP droplets develop heterogeneous skins prone to localized cracking. These observations are further rationalized by comparison with model colloid–polymer films, allowing us to establish a mechanistic link between interfacial mechanics, skin formation, and drying-induced instabilities.[28]

B Experimental

1 Materials

– Protein solutions: native phosphocaseinate (NPC) and napin (NAP) suspensions with 3 wt% total protein concentration were prepared by dissolving NPC (commercial powder, 82% protein content) and NAP (in-house purified, 94% protein content) in deionized water containing 0.02 wt% of sodium azide (NaN_3) as a bacteriostatic agent and stirred overnight to ensure complete hydration of the protein. Typical sizes of NPC and NAP are 100–300[17] and 2 nm,[19] respectively.

The interfacial tension at $T = 25$ °C of NAP and NPC at 3 wt% was determined using the hanging drop method with a drop tensiometer (Tracker, IT Concept, Longessaigne, France). A 100 μL syringe was filled with the protein solution and connected to a needle. A drop of liquid was formed at the tip of the needle immersed in a 5 mL glass cuvette. The volume of the drop was 10 μL. The shape of the drop was recorded using a CCD camera and the data were recorded for 1 hour. The air–water interfacial tension, γ, was calculated using the Young–Laplace equation:

$$\Delta P = \gamma \cdot (1/R + 1/R') \quad (1)$$

where R and R' are the principal radii of curvature of the drops and ΔP is the Laplace pressure corresponding to the pressure difference across the interface. At equilibrium, the measured surface tension values were 41 ± 5 mN m^{-1} for the NAP solution and 48 ± 5 mN m^{-1} for the NPC solution.

– Model systems: they were used to mimic the mechanical properties of protein films and the related mechanical instabilities, *e.g.*, crack patterns observed. Hence, we consider composite systems made of nanosilica particles and polymers to tune the mechanical properties of films.[15] An aqueous suspension of nearly spherical silica colloids was used (Ludox TM-50) commercially available from Sigma-Aldrich. The particle diameter and the polydispersity are reported to be 25 nm and 0.14, respectively.[29] The solid weight content was 50 wt% corresponding to a volume fraction of 0.30. The silica suspensions were mixed with polyvinylpyrrolidone (PVP).[30] The molecular weight of PVP was 40 kDa, commercially available from Sigma-Aldrich. The polymer concentrations were kept below 0.01 mg m^{-2}, to ensure partial coverage of the particles. A solution with a polymer weight concentration denoted as C_p was added to a TM-50 suspension, denoted as C_c. After dilution, the final polymer concentration in the TM-50 dispersion is $C_p/4$. Within this concentration range, polymers adsorb onto particles to form

necklace-like structures, resulting in a stable dispersed state due to repulsive interactions between these necklaces. In this way, the mechanical properties of the dried composite film denoted by TM/PVP, ranging from brittle to ductile, depend on the polymer content added to the colloidal suspension.

2 Methods

The acoustic levitator consists of two opposing transducer arrays, arranged in a concave geometry to focus the acoustic wave. The model used here is Mk1 from ref. 15. A similar acoustic levitator has been used to study interfacial phenomena and measure the surface tension.[4] This type of acoustic levitator presents the advantage of inducing a minimal internal flow,[31] which would disrupt the drying process. This assumption is consistent with the theoretical and experimental analyses of internal flows in acoustically levitated droplets reported in ref. 31, which shows that, for millimetric droplets trapped at a pressure node and moderate acoustic amplitudes, acoustic streaming remains weak and does not significantly affect solute transport during slow evaporation. A droplet ($V \approx 4$ μL) is introduced using an automatic pipette at a node of the standing wave. At time $t = 0$, the droplet is no longer attached to the automatic pipette. The droplet therefore remains suspended until the dried residue of the droplet is collected for microscopy observations. The whole system is enclosed in a chamber to allow for a controlled environment (temperature and humidity). The evaporation is controlled by the diffusion of vapor into the surrounding air. The droplet evolution is captured during evaporation using a camera positioned for the side view and a homemade software allowing the calculations from each image of the geometrical parameters of the droplet (area, length, width, and thickness) (Fig. S1).

The mechanical properties of the samples are evaluated with nanoindentation using a UNHT3 nanoindentation tester[32] (Anton Paar). These measurements were conducted on NAP, NPC, and model systems (TM-50/PVP). All systems were deposited in liquid form on a microscope glass slide. The formation of the film occurred under ambient conditions. Mechanical properties of the solid layers were measured two hours after deposition to ensure consistency in the solidification conditions.

For scanning electron microscopy, dried droplets were deposited onto an adhesive carbon pad, dried at room temperature and observed with a Phenom Pure lab bench scanning electron microscope (Thermo Scientific). Several images are recorded using the following parameters: a full backscattered detector (BSD), a pressure of 1.1 Pa, a high voltage (HV) of 10 kV, beam intensity (Int.) set to image and at different magnifications (×330 and ×500).

C Results and discussion

1 Drying dynamics of protein droplets under substrate-free conditions

In the following, we focus on acoustically levitated droplets, which provide a substrate-free geometry and allow direct access to evaporation-driven mechanical instabilities without contact-line effects. For comparison, it is useful to briefly recall the classical case of a droplet evaporating on a flat substrate (Fig. 1(a)).

In the sessile configuration, the vapor concentration field around the droplet is distorted by the presence of the solid boundary. Indeed, the surfaces of equal vapor concentration are not spherical, since the boundary condition imposed by the substrate requires these surfaces to be perpendicular to the solid surface. Approximate polynomial solutions describing this evaporation field have been proposed, with deviations from the exact solution of less than 0.1%. This leads to an average evaporation rate of the droplet V_E given by[33]

$$V_E = f(\theta_0)\frac{D_w}{R_b}\left(\frac{n_{ws} - n_{w\infty}}{n_1}\right) \quad (2)$$

where $f(\theta_0)$ is the dimensionless numerical factor that accounts for the shape of the droplet, mainly the contact angle, θ_0 (for a contact angle between 15° and 45°, this factor is almost constant and around 1.3),[34] D_w is the diffusion coefficient of water into air, and R_b is the radius of the base of the droplet (Fig. 1(a)). The quantities $n_{w\infty}$ and n_{ws} are the water concentrations in air at infinity and at saturation, and n_1 is the number of water molecules per unit volume in liquid water. These quantities

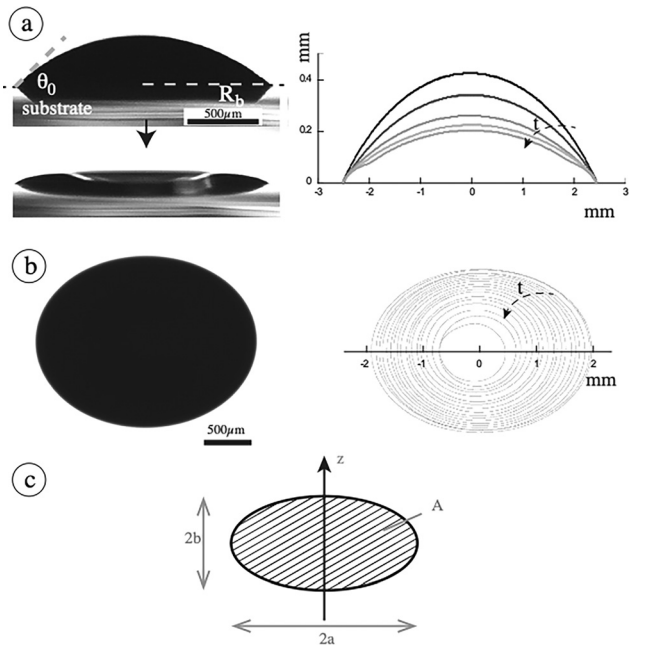

Fig. 1 (a) Left: Lateral views showing the initial state and the final state of a droplet deposited on a glass slide, NPC droplet 3 wt%. The droplet/substrate contact base remains constant during drying (the visual effect of the point at the droplet edge is due to the reflection of the droplet on the substrate). Right: Superposition of droplet profiles during drying. Only the first profiles are shown for clarity. (b) Left: Image after deposition and stabilization of a levitated NPC droplet (3 wt%) in a standing wave field (scale bar: 500 μm). Right: The superposition of digitized images taken at different times highlighting the evolution of droplet profiles during the drying process. (c) Sketch of the oblate spheroid.

are related through the humidity, RH, of the surrounding environment.

In contrast, an acoustically levitated droplet does not encounter any solid boundaries (Fig. 1(b)). The evaporation field is therefore closer to that of an isolated droplet, and the evaporation rate can be written as follows:

$$V_E = \frac{D_w}{R_0}\left(\frac{n_{ws} - n_{w\infty}}{n_1}\right) \quad (3)$$

where R_0 is the initial mean radius of the levitated droplet. The drying process is characterized by a drying timescale, t_D, defined from the droplet size and the evaporation rate. For droplet sizes smaller than the capillary length, gravity does not significantly affect the shape. In this regime, the characteristic length is the radius of the droplet contact base on the substrate, while it is the droplet radius in the case of a levitated droplet. Acoustically levitated droplets, however, often adopt an oblate shape due to the acoustic confinement. For an oblate shape of revolution, the evaporation timescale is expected to be shorter than that of a spherical droplet of identical volume, owing to the increased surface area and reduced diffusion path along the minor axis. We therefore define the drying timescale as[35]

$$t_D = \frac{b}{V_E} \quad (4)$$

where b is the semi-minor axis (along the axis of revolution).

Although the evaporation rates of sessile and levitated droplets are comparable, the absence of contact-line pinning in levitated droplets fundamentally alters solute transport and shape evolution, which motivates the use of acoustic levitation to study the intrinsic dynamics of drying.

The evolution of droplet shape during evaporation is monitored using transmitted-light imaging. Assuming axisymmetry, this technique enables direct measurement of the droplet cross-sectional area A, as illustrated in Fig. 1(c). Prior to the onset of mechanical instabilities, discussed in Section C.3, the droplet maintains rotational symmetry about the vertical axis z, which lies in the plane of the measured cross-section. In this regime, the droplet shape is well approximated by an oblate spheroid with the semi-major axis a (in the equatorial plane) and the semi-minor axis b. The droplet volume is then given by

$$V = \frac{4}{3}\pi a^2 b \quad (5)$$

The oblate shape is characterized by the eccentricity, e, which is defined as

$$e = \sqrt{1 - \frac{b^2}{a^2}} \quad (6)$$

In the approximation of a droplet with low eccentricity, the total surface area of a slightly oblate spheroid is expressed as follows:

$$S \approx 4\pi a^2\left(1 - \frac{e^2}{6}\right) \quad (7)$$

From the measured cross-sectional area and the extracted values of a and b, both the total surface area S and the volume V can be deduced under the axisymmetric assumption of the droplets.

Fig. 2(a) shows the temporal evolution of the normalized surface area S/S_0 and volume V/V_0 for both a sessile droplet and an acoustically levitated droplet of NPC at 3 wt% total protein

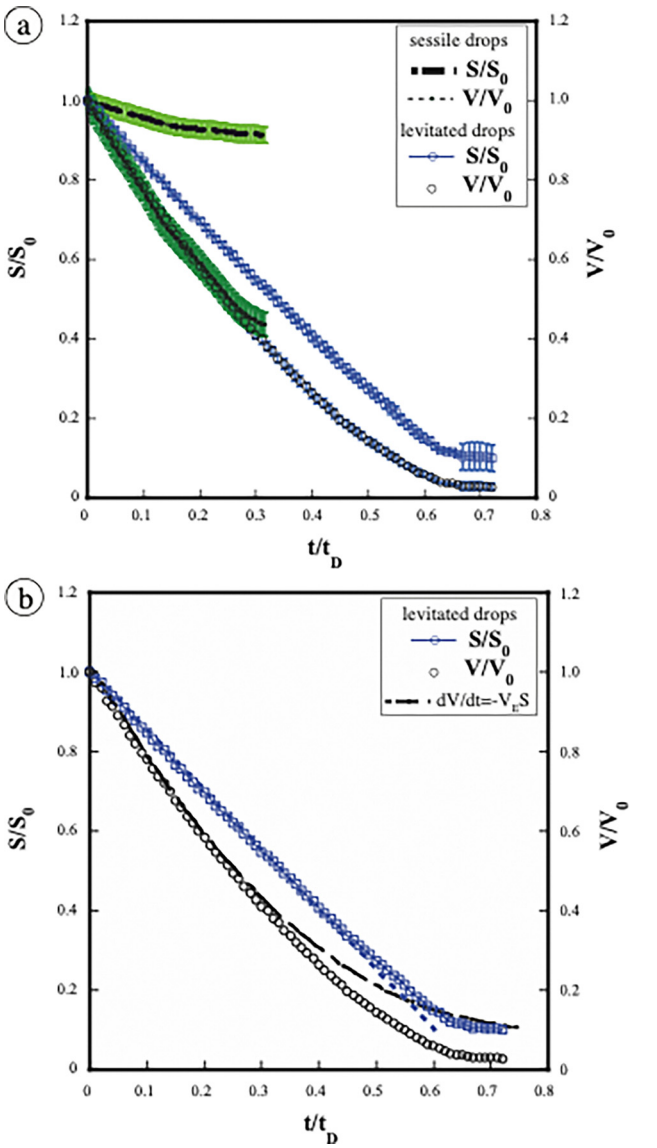

Fig. 2 (a) Time evolution of the dimensionless surface area and dimensionless volume for native phosphocaseinate (NPC) droplets (3 wt%), comparing sessile and acoustically levitated drying configurations. Data are averaged over three independent droplets per condition. Symbols represent mean values, and error bars indicate the standard deviation (green error bars indicate the standard deviation of the surface area and volume of sessile drops). Time is normalized by the characteristic drying time t_D defined in eqn (4). S_0 and V_0 denote the initial surface area and volume at t = 0. The initial volumes are 4.1 ± 0.2 mm^3 for sessile droplets and 3.9 ± 0.2 mm^3 for levitated droplets. (b) Time evolution of the dimensionless surface area and dimensionless volume for acoustically levitated NPC droplets (3 wt%), averaged over three independent droplets, together with the volume evolution deduced from eqn (9). Symbols represent mean values with error bars indicating the standard deviation. The dashed line is a linear guide to the eye.

concentration. At short times, the volume evolution is similar in both configurations, consistent with diffusion-limited evaporation. In contrast, the surface area of the sessile droplet decreases much more slowly due to contact-line pinning at the substrate. This difference highlights the advantage of acoustic levitation for probing intrinsic shape relaxation during drying, free from substrate-induced constraints.

Beyond this global behaviour, the influence of protein type on the geometric evolution of drying droplets can be quantified. The drying dynamics of droplets composed of NPC and NAP proteins are analysed by monitoring the temporal evolution of their surface area. For both systems, the surface area decreases nearly linearly with time before reaching a plateau at the final stage of drying (Fig. 3b).

The initial cross-sectional areas are reported in Table 1 and shown in Fig. 3a. Notably, the drying curves for NAP droplets exhibit significantly larger dispersion than those of NPC droplets (Fig. 3b). This variability can be attributed to differences in the initial droplet shape: NAP droplets are more flattened immediately after levitation than NPC droplets, as evidenced by the droplet profiles and cross-sectional images (Fig. 3a). This behaviour is consistent with the distinct interfacial properties of the two proteins (Section B.1). The shape of a levitated droplet is determined by the balance between surface tension, gravity, and acoustic forces. A high surface tension favours an almost spherical shape, while a lower surface tension causes flattening or elongation along the acoustic pressure gradient and can reinforce internal flows and instabilities during evaporation.

To account for these shape differences, the characteristic drying time t_D is introduced. Rescaling the data using t_D leads to a markedly improved collapse of the drying curves, as shown in the inset of Fig. 3b.

In addition, the circularity, C, quantifies how close the shape is to a circle. This parameter is classically defined using the ratio between the area of the droplet's projected shape, A, and its perimeter, l, as

$$C = 4\pi A/l^2 \tag{8}$$

The evolution of the droplet during the drying process is characterized by an increase in circularity, regardless of the droplet type. However, the circularity is, on average, greater for NPC droplets compared to NAP droplets (Fig. 3c). As evaporation progresses and the size of droplets decreases, the balance of forces governing the shape of the droplets evolves: acoustic confinement weakens while capillary effects become increasingly dominant. As a result, the droplets gradually relax to adopt a spherical geometry. A quantitative analysis of the forces involved in droplet stability is presented in Section C.2.

The dynamics of the drying process involves the decrease of the droplet volume, $V(t)$, due to evaporation as follows:[35]

$$\frac{dV}{dt} = -V_E S \tag{9}$$

From the lateral surface area, S, deduced from the direct measurements of the quantities a and b, the volume, V, of a

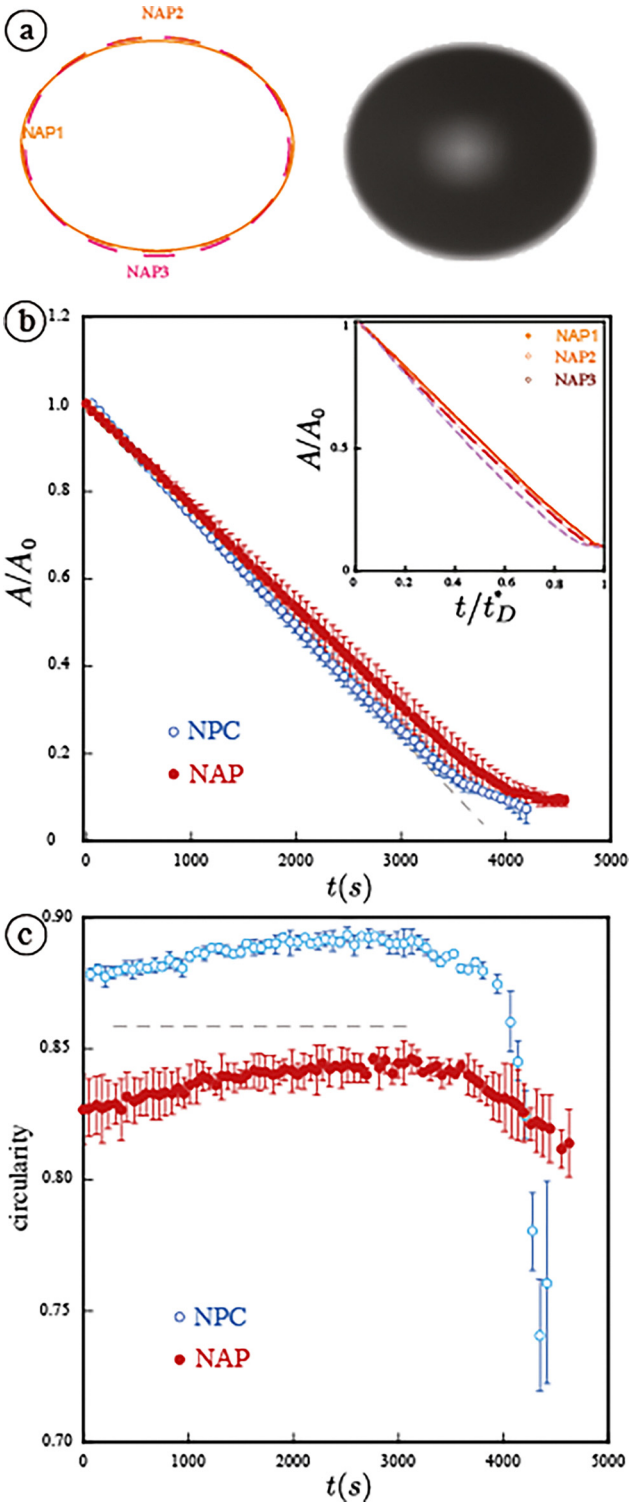

Fig. 3 (a) Representative cross-sectional images of acoustically levitated protein droplets just after deposition: NAP (right) and NPC (left). (b) Time evolution of the dimensionless cross-sectional area, A/A_0, during drying for three independent droplets of NAP and NPC. Symbols represent the mean values, while the error bars indicate the standard deviation. Inset: Time is expressed in dimensionless form using the characteristic drying time t_D, calculated from the instantaneous evaporation surface area of the droplet. (c) Time evolution of the droplet circularity during drying for NAP and NPC, averaged over three independent droplets, with error bars representing the standard deviation.

Table 1 Cross-sectional surface area of NAP and NPC droplets. A_0 is the cross-sectional surface area measured at t = 0, immediately after droplet deposition for various droplets. t_B is the buckling time defined by the change in the evolution of the droplet's circularity and it corresponds to the timescale when the slope of the circularity becomes horizontal. The droplet radius, R_c, at buckling is estimated at the vertical semi-major axis, b. The elastic modulus, E, is estimated from the buckling onset, as described in Section C.2, while the quantity, E^*, is the elastic modulus measured using indentation testing from dried films of NAP and NPC

		A_0 (mm^2)	$t_B \pm 30$ (s)	$R_c = b \pm 0.02$ (mm)	$E \pm 0.1$ (MPa)	$E^* \pm 1.2$ (MPa)
NAP	1	12.2	3900	0.33	1.8	3.5
	2	12.4	4150	0.34	1.7	4.0
	3	11.9	3840	0.31	1.6	3.8
	4	12.5	3960	0.32	1.6	3.5
NPC	1	13.0	2420	0.66	2.4	5.2
	2	13.1	2160	0.71	2.7	6.1
	3	12.9	2280	0.67	2.2	5.9

levitating droplet, in accordance with eqn (9), is compared to the volume directly estimated from quantities a and b in Fig. 2(b). The good agreement at short times highlights an evaporation process limited by the diffusion of water into the air, as already seen in the literature.[36] Beyond this initial evaporation-controlled regime, deviations from purely geometric relaxation indicate the emergence of interfacial consolidation, which is discussed in the following section.

2 Shape evolution and interfacial skin formation during evaporation

As evaporation progresses beyond the initial diffusion-limited regime, the droplet's shape begins to deviate from the purely geometric relaxation described in C.1. These deviations indicate the formation of a denser, partially consolidated layer at the droplet–air interface, which we call the interfacial ''skin.'' This skin arises from the accumulation of non-volatile protein components near the evaporation surface, which reduces local mobility and partially protects the internal liquid core from further deformation.

In levitated droplets, several forces act to maintain both the droplet's shape and its position within the acoustic field. The dominant forces are as follows:

– The acoustic radiation force F_a that acts on a droplet of volume V is expressed as[37]

$$F_a = Vk\frac{\phi}{3}\frac{p^2}{\rho c^2} \tag{10}$$

where k is the wave number that accounts for the gradient of the energy density in a standing wave field, ϕ is the acoustic contrast factor related to the acoustic impedance mismatch ($\sim$0.5), p is the acoustic pressure ($\sim 10^3$ Pa), ρ is the density of the surrounding air, and c is the speed of sound in the air (c = 343 m s^{-1}).

– This force balances the gravitational force:

$$F_g = V\rho_l g \tag{11}$$

for a droplet of density ρ_l. For a droplet size of 1 mm, k = 730 m^{-1}, $p = 5 \times 10^3$ Pa, and the gravitational force and the acoustic force are $\sim 4 \times 10^{-2}$ mN.[7] This competition stabilizes the droplet position.

– The gravitational force impacts the droplet shape when the droplet size is larger than the capillary length. Hence, we deal with droplet sizes smaller than the capillary length. However, the acoustic radiation force F_{cap} competes with the surface tension force:

$$F_{cap} = 2\pi\gamma \cdot r \tag{12}$$

where γ is the surface tension, and r is the droplet size ($F_{cap} \approx 7 \times 10^{-2}$ mN). When the acoustic force approaches or exceeds the capillary force, droplet deformation can occur. This possibly results in an oblate shape with a flattening at the poles as shown in Fig. 1b.

Initially, larger droplets experience stronger acoustic forces owing to the limited space of the acoustic nodes where they lie. However, as evaporation reduces the droplet radius, the capillary force becomes more significant and makes the droplet increasingly closer to a sphere.[38] Potentially, shape distortions governed by mechanical instability take place when a solid skin forms at the droplet/air interface. As evidence, the superposition of profiles taken at different times during the drying process of NPC is shown in Fig. 1b. Starting from an oblate shape, the droplet continuously approaches a spherical shape during its retraction induced by the drying process.

Monitoring the circularity provides further insight into shape evolution. Initially, circularity increases as the droplet relaxes toward a sphere. At later stages, however, the circularity no longer grows monotonically but takes on irregular values (Fig. 3c). This irregularity reveals a more complex droplet shape, reflecting the evolving internal dynamics: redistribution of non-volatile solutes, formation of the skin, and local stress accumulation within the droplet.

This transition originates from the redistribution of non-volatile solutes during evaporation. Initially, proteins are homogeneously dispersed within the droplet. As the solvent evaporates, capillary flow transports these solutes toward the interface to replenish the evaporating liquid, leading to the formation of a concentration gradient. Progressive accumulation of proteins near the surface results in the formation of a porous, solid-like skin. The droplet thus progressively adopts a ''capsule'' structure, consisting of a solid shell of thickness h, density ρ_s, and radius R, enclosing a still-liquid core.

Although permeable to water, this interfacial skin increasingly resists deformation. As its thickness grows, the skin partially screens capillary forces and begins to sustain mechanical stresses generated by continued evaporation. During this stage, and following the evolution described by eqn (9), the shell thickness increases proportionally to the evaporation rate according to[31–41]

$$\frac{dh}{dt} \sim V_E\left(1 - \phi_g\right) \tag{13}$$

where V_E is the evaporation rate. The parameter ϕ_g is introduced as an effective volume fraction characterizing the formation of a

mechanically coherent interfacial layer. For protein systems, this quantity should not be interpreted as a geometrical close-packing fraction of rigid particles, but rather as an effective parameter describing a hydrated, deformable, and porous protein network. Variations of ϕ_g within a realistic range for hydrated protein assemblies primarily rescale the estimated shell thickness and the effective elastic modulus inferred from buckling, without affecting the qualitative trends or the relative comparison between NAP and NPC droplets. Consequently, the elastic moduli extracted from the buckling analysis should be regarded as effective poroelastic parameters of the interfacial skin at the onset of instability, rather than intrinsic solid-state moduli.

As drying proceeds, several forces act on this forming shell. The gravitational force F_g on the shell can be expressed as

$$F_g = 4\pi R^2 h \rho_s g, \tag{14}$$

in accordance with eqn (11), while the in-plane compressive force generated by capillary pressure is given by:[42]

$$F_{cap}^{skin} = P_{cap} R h \tag{15}$$

where the capillary pressure[2] at the porous interface scales as $P_{cap} \approx 5\gamma/r_p$, with r_p the typical pore size. For a typical droplet with R = 1 mm and h = 10 μm, the gravitational force scales as $F_g \approx 6 \times 10^{-3}$ mN, which is negligible compared to the capillary force $F_{cap}^{skin} \approx 10$ mN (assuming a pore size $a \approx 10$ nm). Consequently, once the solid shell can no longer sustain the compressive stresses induced by capillary pressure, the buckling process occurs. Hence, the condition for buckling can be expressed as

$$P_{cap} = \sigma_c \tag{16}$$

where σ_c is the critical buckling stress of a thin elastic shell. For a shell of thickness h_c small compared to the droplet radius R_c, this critical stress is given by[42,43]

$$\sigma_c = E\left(\frac{h_c}{R_c}\right)^2 \tag{17}$$

with E the elastic modulus of the shell. Buckling thus arises when a critical combination of shell radius R_c and thickness h_c is reached. Buckling occurs only after a characteristic delay time, t_B, corresponding to the period required for the formation of a solid shell of finite thickness and for sufficient compressive stress to accumulate within it. By combining eqn (13), (16) and (17), the characteristic buckling time can be expressed as follows:

$$t_B = \frac{R_c}{V_E\left(1-\phi_g\right)}\sqrt{\frac{P_{cap}}{E}} \tag{18}$$

This relation shows that the buckling time t_B increases as the elastic modulus E of the solid shell decreases.

Experimentally, the buckling time t_B is identified from the circularity evolution as the point where the circularity curve flattens (Fig. 3(c)), corresponding to the onset of curvature inversion. Although buckling could, in principle, initiate anywhere on the droplet surface, deformation is consistently observed to start at a single pole. Despite this localized instability, the droplet remains stably levitated and globally axisymmetric. Measured buckling times are $t_B \approx 2 \times 10^3$ s for NPC droplets and $t_B \approx 4 \times 10^3$ s for NAP droplets (Table 1). According to eqn (18), a shorter buckling time corresponds to a stiffer shell under identical evaporation conditions. The earlier buckling of NPC droplets therefore indicates a higher shell stiffness compared to NAP droplets, consistent with the elastic moduli reported in Table 1. These trends agree with independent indentation measurements performed on fully dried films (Section B.2 and Fig. S.3). The elastic moduli measured after complete drying, E^*, are systematically higher than those inferred at the buckling onset, E, reflecting the progressive stiffening of the protein network during evaporation.

Beyond the onset of buckling, the shell undergoes a curvature inversion that produces a persistent circular fold (Fig. 4). The characteristic fold size, δ, results from the balance between bending and stretching energies and scales as[44]

$$\delta \sim \sqrt{\rho h} \tag{19}$$

Analysis of this folding geometry allows an independent estimate of the shell thickness at buckling, yielding $h_c = 54 \pm 5$ μm for NPC droplets and $h_c = 124 \pm 5$ μm for NAP droplets. These values further highlight the distinct mechanical pathways followed by the two protein systems during drying.

3 Final mechanical response of the interfacial skin: fracture *vs.* ductility

As shown in Section C.2, evaporation induces the progressive formation and stiffening of an interfacial protein skin, which eventually undergoes buckling once compressive stresses exceed its elastic resistance. Beyond this mechanical instability, further evaporation proceeds under conditions where geometric

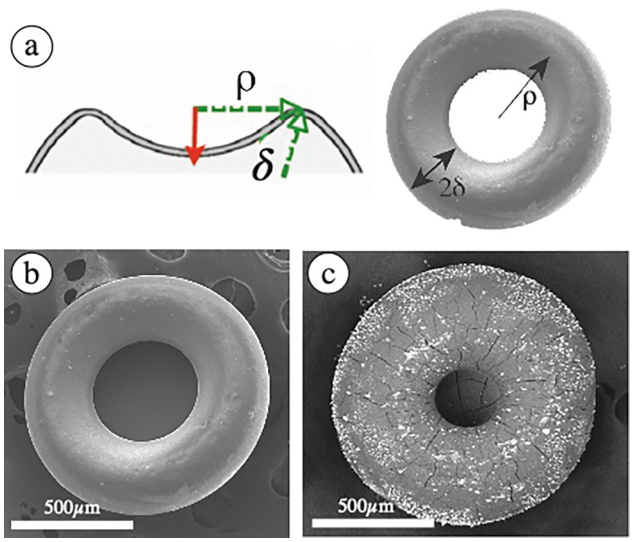

Fig. 4 (a) Schematic representation of a peripheral fold of size δ formed during curvature inversion. (b) and (c) Images of droplets at the final stage of drying: (b) NPC 3 wt% and (c) NAP 3 wt%.

relaxation is no longer sufficient to accommodate the increasing tensile stresses within the skin. In this late regime, the final surface morphology of the droplet is governed by the mechanical response of the solidified shell. Depending on the nature of the protein network, stress relaxation may occur either through fracture or through distributed, ductile (or viscoelastic) deformation without cracking. The crack patterns observed at the end of drying therefore provide a direct signature of the skin's mechanical properties at the final stages of evaporation, as well as of the presence of heterogeneities that can act as nucleation sites.

A striking contrast is observed between NAP and NPC droplets: while the surface of NAP droplets displays cracks and localized white spots (Fig. 4c), NPC droplets dry without any detectable cracking (Fig. 4b). The white spots observed in NAP droplets likely correspond to nucleation centers, although the exact nature of these nuclei remains unclear. In fact, the use of a dye showed that these white spots did not correspond to crystalline protein nuclei. We believe that they are instead heterogeneities originating from the protein sample. When using plant proteins, it is very common to identify different isoforms of the same protein or residual salts in samples after extraction and purification.

To rationalize these observations, we compared protein droplets with model films composed of nanosilica particles (TM-50) and polyvinylpyrrolidone (PVP), chosen for their film-forming properties and their ability to mimic the ''skin'' of a drying droplet. Thin films of TM/PVP were prepared by blade-coating aqueous solutions on glass substrates, with the gap between the blade and substrate adjusted to yield a dried film thickness comparable to that of dried droplets (as estimated in Section C.2). Upon solvent evaporation under ambient conditions, the concentration of solutes increases, and a solid film forms. As drying proceeds, differential shrinkage between the outer skin and the inner phase generates tensile stresses that may drive crack formation (Fig. 5).

Pure nanosilica films exhibit hierarchical crack networks typical of brittle materials. The addition of PVP progressively suppresses cracking: increasing the polymer content enlarges the characteristic cell size, and above a critical concentration (C_p = 0.33), films remain crack-free. This behaviour closely resembles the crack-free surface observed for NPC droplets. Conversely, starting from a nanosilica film with a low PVP content (C_p = 0.15), which is usually crack-free, the addition of a small fraction of cerium oxide nanoparticles (a few hundred nanometres in size) reintroduces cracks by providing nucleation sites. However, the increased ductility imparted by PVP prevents cracks from propagating, resulting in isolated, non-connected cracks (Fig. 5).

This pattern strongly resembles that of NAP droplets: a heterogeneous material containing multiple nucleation sites, but with mechanical properties that hinder crack propagation. In levitated NAP droplets, cracks are preferentially observed near the poles, where curvature variations are larger and where local evaporation rates are expected to be enhanced. These geometric and transport effects promote earlier stress accumulation within the solidified skin, favouring crack nucleation in these regions. This interpretation is further supported by

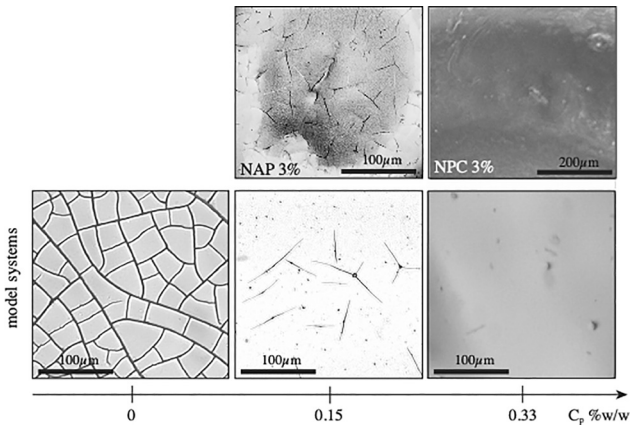

Fig. 5 Zoomed-in views of crack patterns at the surface of the droplet at the final stage of drying for NAP and NPC droplets. The crack morphologies are similar to the patterns formed during drying of model systems made of Ludox TM-50 and polyvinylpyrrolidone (PVP). C_p is the concentration of the solution of PVP added to the suspension of nanosilica particles (wt%).

indentation testing (Fig. S.3). Increasing the PVP concentration reduces the elastic modulus of the film, reflecting the weaker particle–particle interactions and the predominance of the softer polymer matrix. Qualitatively, a higher polymer content corresponds to lower stiffness, greater ductility, and deeper indentation at equal applied force. By tuning the nanosilica/PVP ratio, the macroscopic response of model films can be made analogous to that of protein droplets. It is important to emphasize that the elastic modulus of the interfacial skin is not expected to increase smoothly or linearly during drying. In contrast, previous indentation measurements on drying colloidal skins have shown that the Young's modulus can evolve in a strongly nonlinear manner, often following a power-law increase as consolidation proceeds. In this context, the modulus extracted at the onset of buckling should be regarded as an effective, instantaneous modulus characterizing the mechanical state of the skin at the instability threshold, rather than as a time-averaged or continuously evolving quantity. Importantly, the buckling analysis does not require detailed knowledge of the full temporal evolution of the elastic properties, but relies only on the mechanical response at the moment when compressive stresses overcome the elastic resistance of the skin.

Finally, these insights can be extended to mixed protein droplets (Fig. 6). NAP proteins impart fragility, favouring crack initiation, whereas NPC proteins confer ductility and suppress cracking. As a result, crack and wrinkle patterns at the droplet surface arise from the balance of these two contributions. Importantly, the observed patterns can be reproduced in model systems, thereby establishing a direct link between the microscopic composition, mechanical response, and macroscopic drying instabilities.

4 Discussion

The drying of protein droplets follows a continuous, time-dependent sequence that combines evaporation, solute

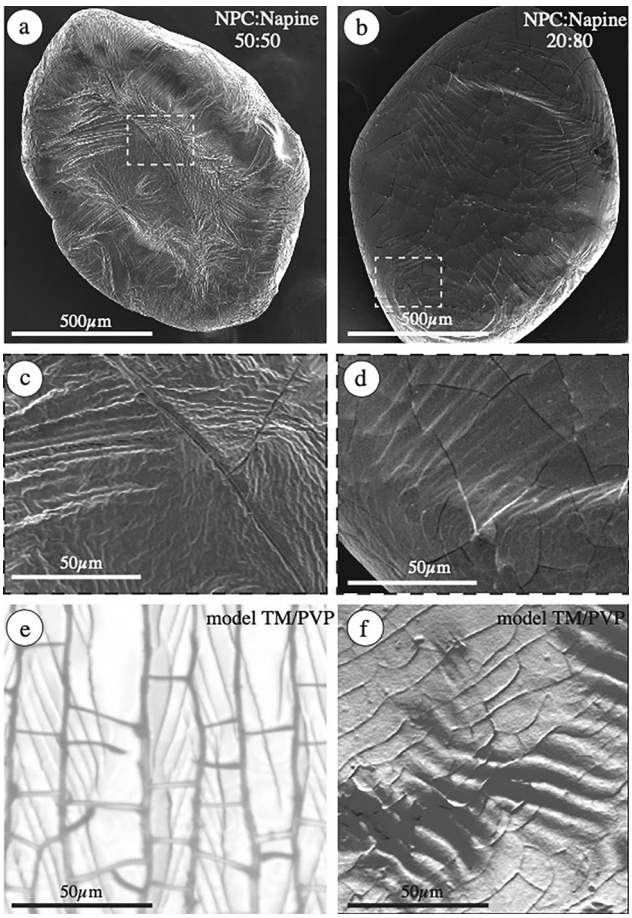

Fig. 6 Dried droplets of various mixtures of NAP and NPC at 50 : 50 (a) and 20 : 80 (b) ratios. The surface patterns (corresponding zoomed-in views in (c) and (d)) exhibit cracks and wrinkles, which can be observed in films of model systems composed of silica TM and PVP (e) and (f).

transport, interfacial consolidation, and mechanical instabilities. At early times, evaporation is diffusion-limited and the droplet behaves as a simple liquid, whose shape relaxes smoothly under capillary forces and, for levitated droplets, acoustic confinement. This initial regime is well described by geometric considerations alone. As evaporation proceeds, non-volatile proteins are advected toward the droplet–air interface, leading to the progressive formation of a protein-rich interfacial skin.

This transition marks a qualitative change in the drying dynamics: the droplet evolves from a liquid body to a liquid core surrounded by a solidifying shell. The shell thickens and stiffens over time while compressive stresses build up due to evaporation-driven shrinkage (Fig. 7). When these stresses exceed the elastic resistance of the shell, buckling instability occurs. Buckling provides a direct, time-resolved signature of skin formation and mechanical stiffening and defines the onset of a mechanically constrained drying regime. Beyond this point, further evaporation generates tensile stresses that can no longer be relaxed by smooth geometric deformation.

In the final stage of drying, the surface morphology is governed by the fracture or ductile response of the interfacial skin. The resulting crack and wrinkle patterns therefore encode the mechanical properties of the protein network and the presence of heterogeneities acting as nucleation sites. A clear contrast is observed between the two protein systems: NPC droplets form relatively homogeneous and ductile skins that relax stresses without fracture, whereas NAP droplets develop heterogeneous skins prone to localized cracking.

The behaviour of model nanosilica–PVP films supports this interpretation by reproducing the full range of observed morphologies through controlled variations of stiffness, ductility, and defect density. Together, these results establish a direct link between the time evolution of interfacial mechanics and the final drying-induced patterns. The schematic timeline shown in Fig. 7 summarizes this drying pathway, from initial evaporation (t = 0) to skin formation, buckling, and long-time crack or wrinkle development.

Conclusions

This study demonstrates the remarkable stability of acoustically levitated droplets over long drying times, enabling for the first time a direct comparison of evaporation-driven instabilities in plant (napin) and dairy (native phosphocaseinate, NPC) protein systems. The contact-free levitation setup ensures symmetric evaporation and preserves axisymmetry throughout drying, even during buckling of the solidified shell. The onset of buckling is governed by the evolving shell geometry, particularly its thickness, and follows the elastic shell theory, allowing

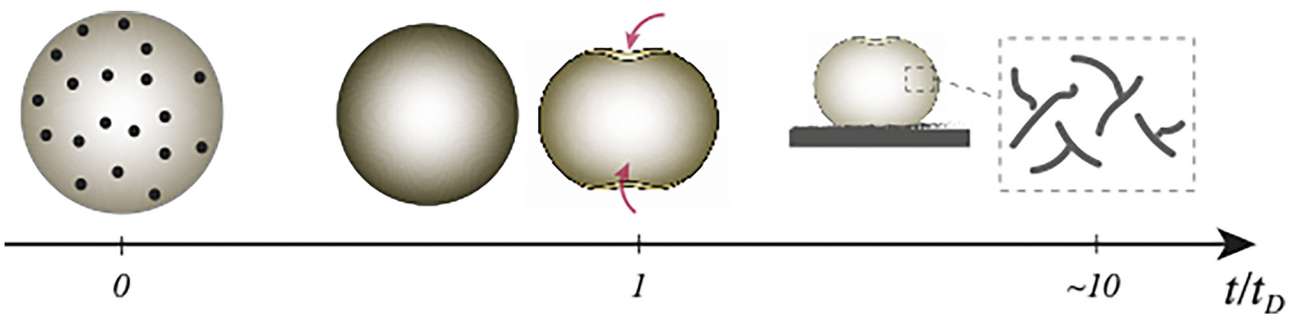

Fig. 7 Schematic illustration of the full drying pathway of an acoustically levitated droplet, from the initial homogeneous liquid state to interfacial skin formation, mechanical instabilities, and the final crack patterns observed at the droplet surface.

estimation of the skin's mechanical properties during formation. At later stages, distinct mechanical responses emerge: napin droplets develop brittle, crack-prone shells, whereas NPC droplets remain ductile and crack-free. These contrasting behaviours reflect fundamental differences in interfacial activity and network formation between plant and dairy proteins. Overall, the results elucidate how protein origin dictates the transition from elastic buckling to fracture, linking interfacial mechanics to drying-induced structure formation. Beyond the model system, this work opens new perspectives for optimizing spray-drying processes and designing sustainable, plant-based protein alternative materials with tailored mechanical and morphological properties.

Conflicts of interest

There are no conflicts to declare.

Data availability

Supplementary information (SI) is available. See DOI: https://doi.org/10.1039/d5sm01113b.

The data supporting the findings of this study are openly available as follows: time-resolved image sequences acquired during the drying of levitated drops can be downloaded from https://sdrive.cnrs.fr/s/6S5dTmKTXjkGEy5 (TIFF format, organized by experiment and acquisition time). Measurements of surface tension for the different solutions investigated are available at https://sdrive.cnrs.fr/s/bd2K4XdFnJA4oiy (xls format). Additional data or analyses, particularly micro-indentation force/displacement data to characterize the mechanical response of the dried films, are available from the corresponding author upon request.

Acknowledgements

The authors acknowledge GDR2019 CNRS/INRAE 'Solliciter LA Matière Molle' (SLAMM).

Notes and references

1 A. Pal, A. Gope and A. Sengupta, *Adv. Colloid Interface Sci.*, 2023, **314**, 102870.
2 F. Giorgiutti-Dauphiné and L. Pauchard, *Eur. Phys. J. E:Soft Matter Biol. Phys.*, 2018, **41**, 32.
3 A. Pal, A. Gope and G. Iannacchione, *Biomolecules*, 2021, **11**(2), 231.
4 R. D. Deegan, O. Bakajin, T. F. Dupont, G. Huber, S. R. Nagel and T. A. Witten, *Nature*, 1997, **389**, 827–829.
5 J. R. Moffat, K. Sefiane and M. E. R. Shanahan, *J. Phys. Chem. B*, 2009, **113**, 8860.
6 J. K. Dewangan, N. Basu and M. Chowdhury, *Soft Matter*, 2022, **18**, 4253–4264.
7 P. Bourrianne, P. Liin, G. Sintès, T. Nîrca, G. H. McKinley and I. Bischofberger, *Soft Matter*, 2021, **17**, 8832–8837.
8 H. M. van der Kooij, G. T. van de Kerkhof and J. Sprakel, *Soft Matter*, 2016, **12**, 2858–2867.
9 M. Yu, C. Le Floch-Fouéré, L. Pauchard, F. Boissel, N. Fu, X. D. Chen, A. Saint-Jalmes, R. Jeantet and L. Lanotte, *Colloids Surf., A*, 2021, **620**, 126560.
10 A. Paul, F. Martin, B. Simard, J. Scher, C. Gaiani, C. Le Floch-Fouéré, R. Jeantet and J. Burgain, *J. Dairy Sci.*, 2023, **106**, 843–851.
11 P. F. Fox and A. Brodkorb, *Int. Dairy J.*, 2008, **18**, 677–684.
12 P. Walstra, *Int. Dairy J.*, 1999, **9**, 189–192.
13 D. S. Horne, *Curr. Opin. Colloid Interface Sci.*, 2006, **11**, 148–153.
14 D. G. Dalgleish, *Soft Matter*, 2011, **7**, 2265–2272.
15 C. G. de Kruif, T. Huppertz, V. S. Urban and A. V. Petukhov, *Adv. Colloid Interface Sci.*, 2012, **171–172**, 36–52.
16 B. Ingham, B. Smialowska, G. D. Erlangga, L. Matia-Merino, N. M. Kirby, C. Wang, R. G. Haverkamp and A. J. Carr, *Soft Matter*, 2016, **12**, 6937–6953.
17 A. Bouchoux, G. Gésan-Guiziou, J. Pérez and B. Cabane, *Biophys. J.*, 2010, **99**, 3754–3762.
18 A. Bouchoux, J. Ventureira, G. Gésan-Guiziou, F. Garnier-Lambrouin, P. Qu, C. Pasquier, S. Pézennec, R. Schweins and B. Cabane, *Soft Matter*, 2015, **11**, 389–399.
19 I. Schmidt, D. Renard, D. Rondeau, P. Richome, Y. Ppineau and M. A.-V. Axelos, *J. Agric. Food Chem.*, 2004, **52**, 5995–6001.
20 A. Boire, A. Bouchoux, S. Bouhallab, A.-L. Chapeau, T. Croguennec, V. Ferraro, V. Lechevalier, P. Menut, S. Pezennec, D. Renard, V. Santé-Lhoutellier, K. Laleg, V. Micard, A. Riaublanc and M. Anton, *Innovative Food Sci. Emerging Technol.*, 2018, **46**, 18–28.
21 A. Boire, D. Renard, A. Bouchoux, S. Pezennec, T. Croguennec, V. Lechevalier, C. Le Floch-Fouéré, S. Bouhallab and P. Menut, *Annu. Rev. Food Sci. Technol.*, 2019, **10**, 521–539.
22 E. B. A. Hinderink, A. Boire, D. Renard, A. Riaublanc, L. M. C. Sagis, K. Schroën, S. Bouhallab, M.-H. Famelart, V. Gagnaire, F. Guyomarch and C. Berton-Carabin, *Curr. Opin. Colloid Interface Sci.*, 2021, **56**, 101507.
23 K. Sridhar, S. Bouhallab, T. Croguennec, D. Renard and V. Lechevalier-Datin, *Crit. Rev. Food Sci. Nutr.*, 2023, 1–16.
24 K. Sridhar, S. Bouhallab, T. Croguennec, D. Renard and V. Lechevalier, *Food Res. Int.*, 2024, **187**, 114419.
25 Z. Duyang, Y. Yinkai Yu, C. Zhen, L. Xiaoguang, W. Hongjing and G. Xingguo, *Adv. Colloid Interface Sci.*, 2017, **243**, 77–85.
26 S.-M. Argyri, C. Andersson, N. Paillet, L. Evenäs, J. Ahrens, A. Marzo, V. Contreras and R. Bordes, *J. Sci.:Adv. Mater. Devices*, 2024, **9**(3), 100720.
27 S.-M. Argyri, L. Evenäs and R. Bordes, *J. Colloid Interface Sci.*, 2023, **640**, 637–646.
28 C. Le Floch-Fouéré, L. Lanotte, R. Jeantet and L. Pauchard, *Soft Matter*, 2019, **15**, 6190–6199.
29 M. Leang, F. Ott, F. Giorgiutti-Dauphiné, L. Pauchard and L.-T. Lee, *J. Colloid Interface Sci.*, 2020, **565**, 474–482.
30 P. Ilekti, PhD thesis, Université Pierre et Marie Curie, 2000.
31 S.-M. Argyri, A. Stark, V. Eriksson, L. Evenäs, A. Martinelli and R. Bordes, *J. Environ. Sci.*, 2025, **158**, 197–206.

32 C. Le Floch-Fouéré, M. Yu, F. Boissel, R. Jeantet, L. Pauchard and L. Lanotte, *Colloids Surf., B*, 2025, **253**, 114761.
33 F. Parisse and C. Allain, *Langmuir*, 1997, **13**, 3598–3602.
34 R. G. Picknett and R. Bexon, *J. Colloid Interface Sci.*, 1977, **61**, 2.
35 L. Pauchard and C. Allain, *Phys. Rev. E:Stat., Nonlinear, Soft Matter Phys.*, 2003, **68**, 052801.
36 A. L. Yarin, G. Brenn, O. Kastner and C. Tropea, *Phys. Fluids*, 2002, **14**, 2289–2298.
37 D. Zang, Y. Yu, Z. Chen, X. Li, H. Wu and X. Geng, *Adv. Colloid Interface Sci.*, 2017, **243**, 77–85.
38 S.-M. Argyri, L. Evenäs, J. Ahrens, A. Marzo, V. Contreras and R. Bordes, *J. Colloid Interface Sci.*, 2023, **629**, 180–188.
39 T. Okuzono, K. Ozawa and M. Doi, *Phys. Rev. Lett.*, 2006, **97**, 136103.
40 D. Sen, J. S. Melo, J. Bahadur, S. Mazumder, S. Bhattacharya, G. Ghosh, D. Dutta and S. F. D'Souza, *Eur. Phys. J. E:Soft Matter Biol. Phys.*, 2010, **31**, 393–402.
41 J. Bahadur, D. Sen, S. Mazumder, S. Bhattacharya, H. Frielinghaus and G. Goerigk, *Langmuir*, 2011, **27**(13), 8404–8414.
42 L. Landau and E. M. Lifshitz, *Theory of Elasticity*, Pergamon Press, New York, 3rd edn, 1986.
43 O. P. Bamboriya and M. S. Tirumkudulu, *Soft Matter*, 2023, **19**, 2605.
44 L. Pauchard and S. Rica, *Philos. Mag. B*, 1998, **78**, 25.

